Supplemental Material: Interference of Temporally Distinguishable Photons Using Frequency-Resolved Detection

Venkata Vikram Orre,[1,2] Elizabeth A. Goldschmidt,[1,3] Abhinav Deshpande,[1,4]
Alexey V. Gorshkov,[1,4] Vincenzo Tamma,[5,6] Mohammad Hafezi,[1,2,7] and Sunil Mittal[1,2]

[1]*Joint Quantum Institute,NIST/University of Maryland, College Park, Maryland 20742, USA*
[2]*Department of Electrical and Computer Engineering and IREAP,*
University of Maryland, College Park, Maryland 20742, USA
[3]*U.S. Army Research Laboratory, Adelphi, MD 20783, USA*
[4]*Joint Center for Quantum Information and Computer Science,*
NIST/University of Maryland, College Park, Maryland 20742, USA
[5]*School of Mathematics and Physics, University of Portsmouth, Portsmouth PO1 3QL, United Kingdom*
[6]*Institute of Cosmology and Gravitation, University of Portsmouth, Portsmouth PO1 3FX, United Kingdom*
[7]*Department of Physics, University of Maryland, College Park, Maryland 20742, USA*

S1: EXPERIMENTAL SETUP

We use type-II SPDC in a 30-mm-long PPKTP crystal to generate two- and four-photons in our experiment. The crystal has a poling period of $46.2~\mu$m and is held at a temperature of $30°$ C. We pump the crystal using a pulsed Ti:sapphire laser ($\approx$80 MHz, 1.6 ps) set at a wavelength of ≈ 775.5 nm such that the spectra of generated photons (≈ 1551 nm) is well within the passband of our CBG ($\approx$533 GHz, centered at 1550.9 nm). Figures S1(a)-S1(c) show the spectra of the horizontally (H) and vertically (V) polarized photons measured using a tunable filter and a superconducting nanowire detector, the joint spectral intensity of the two-photon wavefunction measured using CBG as a time-of-flight spectrometer, and the HOM interference dip. We observe small ellipticity in the JSI that also manifests in the two-photon spectral correlations shown in Fig.2 of the main text. We also note that there is a small mismatch in the spectra of generated photons that reduces the visibility of the HOM interference. The visibility can be improved by spectral filtering or by using a crystal with extended phase matching [1]. Using HOM interference, we estimate the upper bound on the single-photon pulsewidth to be $\approx$1.7 ps [Fig. S1(b)]. This agrees well the value of $\approx$1.55 ps that we estimate by fitting numerical simulation results to the experimentally measured data in the two-photon interference.

The measured two- and four-photon generation rates as a function of pump power are shown in Fig. S2. For the two-photon interference experiment (Fig. 2 of the main text), we used a pump power of 50 mW and the measured two-photon generation rate at the output of the SPDC was $\approx 2.1 \times 10^5$ s^{-1}. For each delay setting, the data was acquired for 12 minutes and the maximum number of coincidence counts (normalization factor) in Figs. 2(a-d) is 313, 277, 267, and 198, respectively, in a 1 GHz frequency bin. For the three-photon interference experiment (Fig. 3 of the main text), we used a pump power of 400 mW and measured a four-photon generation rate of ≈ 8000 s^{-1}. The data in Figs. 3(b)-3(e) was acquired for 270, 270, 180, and 390 minutes, and the maximum number of four-fold coincidence counts (normalization factor) is 325, 286, 289, and 167, respectively, in a 3 GHz frequency bin. For Fig. 4 measurements we pump the SPDC at 100 mW, and each data set was acquired for 20 minutes. The maximum number of counts in Figs. 4(a,b) is 180, in a frequency bin of 1 GHz. The insertion loss of the CBG was measured to be 1.7 dB, and the per-channel excess insertion losses of the fiber beam splitter and the tritter were measured to be $\approx$0.4 dB and $\approx$0.5 dB, respectively.
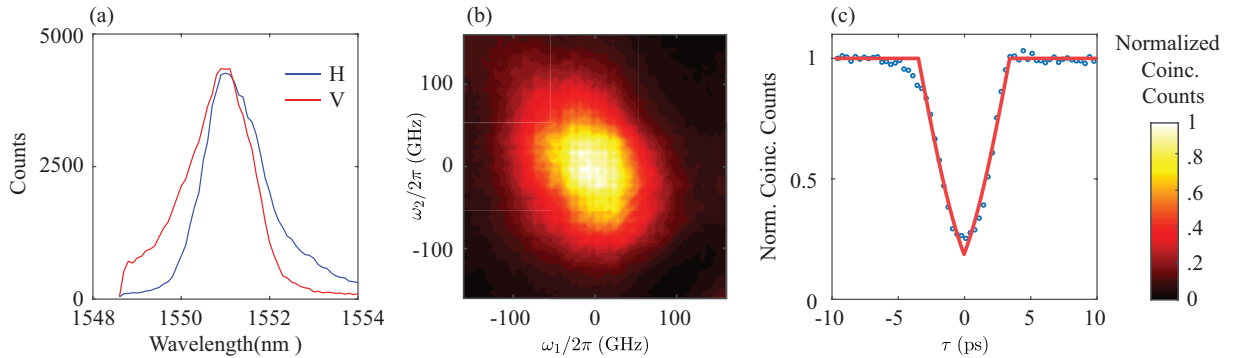
FIG. S1. (a) Measured spectra of H and V polarized photons, (b) joint spectrum intensity (JSI) and, (c) HOM interference dip with a visibility of 82%. The solid curve in (c) is an error function fit to the data [2].
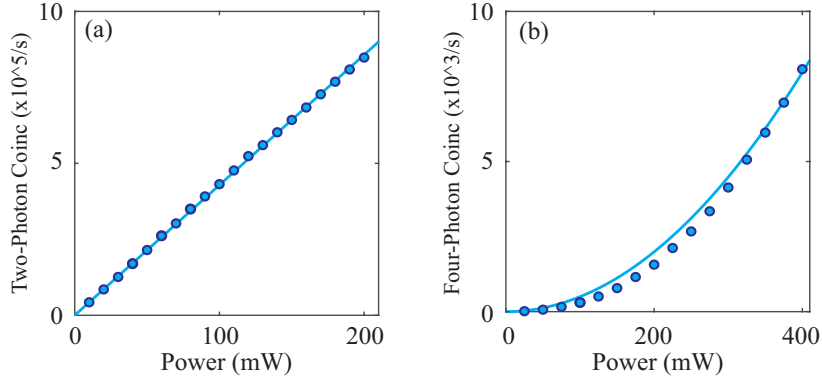
FIG. S2. (a) Measured two-photon and, (b) four-photon generation rates as a function of pump power. The solid lines are linear and quadratic fits to the data, respectively.

S2: FRINGE VISIBILITY IN TWO-PHOTON INTERFERENCE

Figure 2 of the main text shows interference fringes in the normalized coincidence counts as a function of frequency detuning $(\omega_2 - \omega_1)$. From the plot, the interference fringe contrast seems to decrease with the increasing frequency detuning $(\omega_2 - \omega_1)$. This apparent decrease in the contrast is mainly because of the lower coincidence counts as we move away from the center of the two-photon spectral intensity distribution. Therefore, to better estimate the visibility of the interference, we use the ratio of coincidence counts to accidental counts (product of singles counts on the two detectors), shown in Fig. S3(a). We choose a window of 2 ns on each side from the center to further remove the contribution from the edges. Fig. S2(b) shows CAR as a function of $(\omega_2 - \omega_1)$. From this plot, we calculate the fringe visibility as $\left(\overline{I_{\max}} - \overline{I_{\min}}\right) / \left(\overline{I_{\max}} + \overline{I_{\min}}\right)$, where $\overline{I_{\max}}$ and $\overline{I_{\min}}$ are averages of the peak maxima and minima, respectively. We used this visibility measurement scheme for all the data presented in Fig. 2 of the main text.
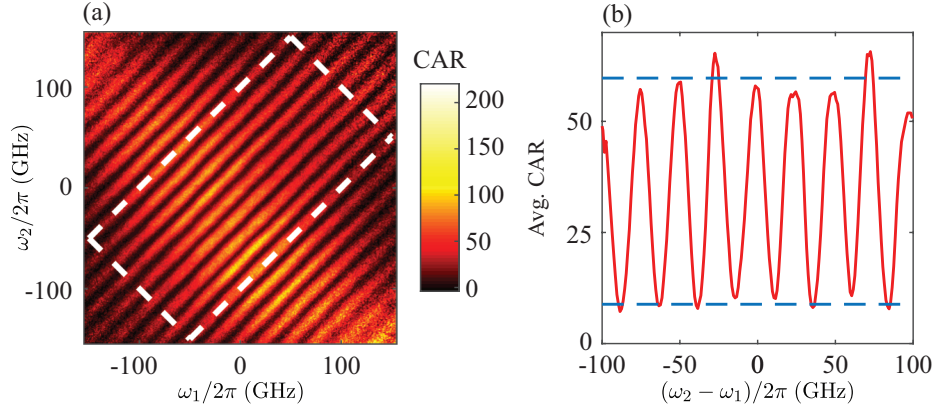
FIG. S3. Measured CAR (a) as a function of ω_1, ω_2 and, (b) as a function of the frequency detuning $(\omega_2 - \omega_1)$, for $\tau = 40$ ps. Blue dotted lines show the mean maximum and minimum of the interference fringes.

S3: MISCELLANEOUS PROBABILITY CONTRIBUTIONS IN THREE-PHOTON INTERFERENCE

Our three-photon interference setup uses one polarization beam splitter and two non-polarizing beam splitters to probabilistically split two pairs of orthogonally polarized photons into four spatial modes (Fig. 3 of the main text). We use one of the modes to trigger the TIA, and use the other three modes along with delay lines and a tritter to achieve a configuration of three photons at times (t_1, t_2, t_3) in one output port of the tritter (before the CBG). Due to the probabilistic nature of beam splitters, three photons with time-delays (t_1, t_1, t_3) and (t_2, t_2, t_3) are also generated with a probability of 0.25, in addition to the desired (t_1, t_2, t_3) events which occur with a probability of 0.5. In Fig. S4 we compare the simulated three-photon interference results,
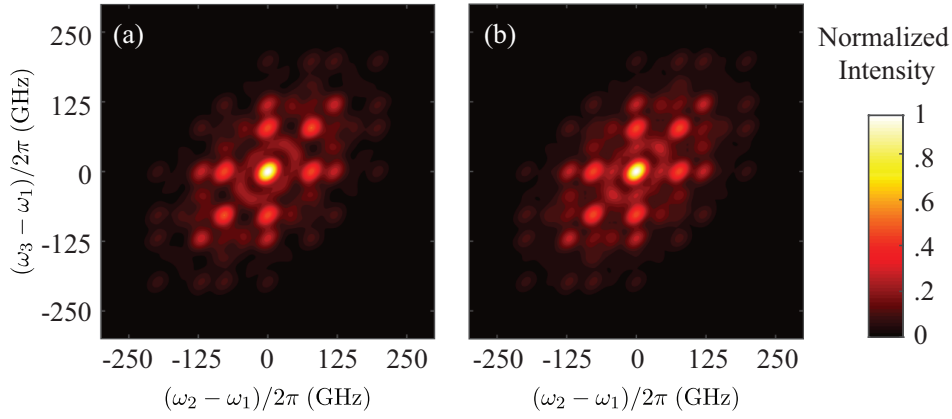
FIG. S4. Simulated three-photon interference, (a) without and, (b) with the extra probability terms, for delays $(\tau_{21}, \tau_{31}) = (10, 25)$ ps.

with and without these unwanted events. As mentioned in the main text, these events do not generate any new beat frequencies and therefore, do not drastically alter the three-photon interference pattern; we observe a fidelity of ≈ 0.99 between the two plots.

S4: REDUCED THREE-PHOTON INTERFERENCE

Here, we show how the integration of the three photon interference over one of the frequencies, reveals information about multiple pairwise interferences. The three-photon correlation function, $\Gamma(\omega_1, \omega_2, \omega_3) = \psi^*(\omega_1, \omega_2, \omega_3)\psi(\omega_1, \omega_2, \omega_3)$ where, $\psi(\omega_1, \omega_2, \omega_3)$ is the three-photon spectral wave function at the detectors, and is associated with the different ways in which three photons with spectral amplitudes E_1, E_2, E_3 at the input, injected at times t_1, t_2, t_3 can trigger the three detectors at frequencies $\omega_1, \omega_2, \omega_3$. It is given as,

$$
\begin{aligned}
\psi(\omega_1, \omega_2, \omega_3) = &\, E_1(\omega_1) E_2(\omega_2) E_3(\omega_3) e^{-i\omega_1 t_1} e^{-i\omega_2 t_2} e^{-i\omega_3 t_3} + E_1(\omega_2) E_2(\omega_1) E_3(\omega_3) e^{-i\omega_2 t_1} e^{-i\omega_1 t_2} e^{-i\omega_3 t_3} \\
&+ E_1(\omega_1) E_2(\omega_3) E_3(\omega_2) e^{-i\omega_1 t_1} e^{-i\omega_3 t_2} e^{-i\omega_2 t_3} + E_1(\omega_2) E_2(\omega_3) E_3(\omega_1) e^{-i\omega_2 t_1} e^{-i\omega_3 t_2} e^{-i\omega_1 t_3} \\
&+ E_1(\omega_3) E_2(\omega_1) E_3(\omega_2) e^{-i\omega_3 t_1} e^{-i\omega_1 t_2} e^{-i\omega_2 t_3} + E_1(\omega_3) E_2(\omega_2) E_3(\omega_1) e^{-i\omega_3 t_1} e^{-i\omega_2 t_2} e^{-i\omega_1 t_3} \quad \text{(S1)}
\end{aligned}
$$

We rewrite the above equation by separating the contribution of ω_3 as,

$$
\psi(\omega_1, \omega_2, \omega_3) = \psi_{12} E_3(\omega_3) e^{-i\omega_3 t_3} + \psi_{13} E_2(\omega_3) e^{-i\omega_3 t_2} + \psi_{23} E_1(\omega_3) e^{-i\omega_3 t_1}. \quad \text{(S2)}
$$

Here

$$
\psi_{ij} = E_i(\omega_1) e^{-i\omega_1 t_i} E_j(\omega_2) e^{-i\omega_2 t_j} + E_j(\omega_1) e^{-i\omega_1 t_j} E_i(\omega_2) e^{-i\omega_2 t_i} \quad \text{(S3)}
$$

such that $\Gamma_{ij} = \left| \psi_{ij}^* \psi_{ij} \right|$ is the two-photon correlation function between photons with input times t_i and t_j respectively and is independent of ω_3. When the three-photon correlation function is integrated over measured frequencies at one of the detectors, here ω_3,

$$
\begin{aligned}
\int_{-\infty}^{\infty} \Gamma(\omega_1, \omega_2, \omega_3)\, d\omega_3 = &\int_{-\infty}^{\infty} \psi^*(\omega_1, \omega_2, \omega_3)\psi(\omega_1, \omega_2, \omega_3)\, d\omega_3 \\
= &\int_{-\infty}^{\infty} \Big[|\psi_{12}|^2 |E_3(\omega_3)|^2 + |\psi_{13}|^2 |E_2(\omega_3)|^2 + |\psi_{23}|^2 |E_1(\omega_3)|^2 \\
&+ \psi_{12}^* \psi_{13} E_3^*(\omega_3) E_2(\omega_3) e^{-i\omega_3(t_2-t_3)} + \psi_{12}^* \psi_{23} E_3^*(\omega_3) E_1(\omega_3) e^{-i\omega_3(t_1-t_3)} \\
&+ \psi_{13}^* \psi_{23} E_2^*(\omega_3) E_1(\omega_3) e^{-i\omega_3(t_1-t_2)} + \text{c.c} \Big] d\omega_3 \quad \text{(S4)}
\end{aligned}
$$

The first three terms are pairwise interferences between photon pairs (1,2), (1,3), (2,3). The remaining terms integrate out to zero, given the single photon spectral wave functions are smooth functions of ω. Therefore, the three-photon spectral correlation function integrated over one of the frequencies is given as

$$
\int_{-\infty}^{\infty} \Gamma(\omega_1, \omega_2, \omega_3)\, d\omega_3 \propto |\psi_{12}|^2 |E_3(\omega_3)|^2 + |\psi_{13}|^2 |E_2(\omega_3)|^2 + |\psi_{23}|^2 |E_1(\omega_3)|^2, \quad \text{(S5)}
$$

$(\tau_{21}, \tau_{31}) \approx (0, 15)$ ps $(\tau_{21}, \tau_{31}) \approx (20, 40)$ ps $(\tau_{21}, \tau_{31}) \approx (10, 25)$ ps $(\tau_{21}, \tau_{31}) \approx (350, 175)$ ps
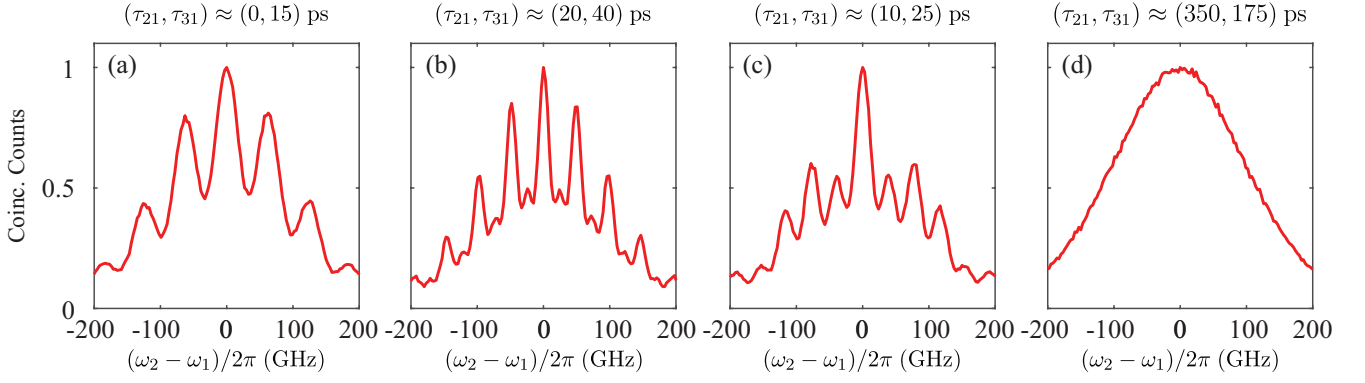
FIG. S5. Measured three-photon correlation function integrated over ω_3, as a function of the frequency separation $(\omega_2 - \omega_1)$ for different delay settings.

where, the intensities of three single-photon spectral wave functions contribute to the weights of the pairwise interferences. Fig. S5 shows the measured three-photon correlation function integrated over ω_3 and plotted as a function of the frequency separation $(\omega_2 - \omega_1)$, for different delay settings. The Fourier transform of these spectra [Figs. 3(j)-3(m) of the main text] show the beat notes corresponding to the multiple pairwise interference terms between the three photons.

S5: GENERATION OF POLARIZATION/TIME-BIN ENTANGLED PHOTON PAIRS
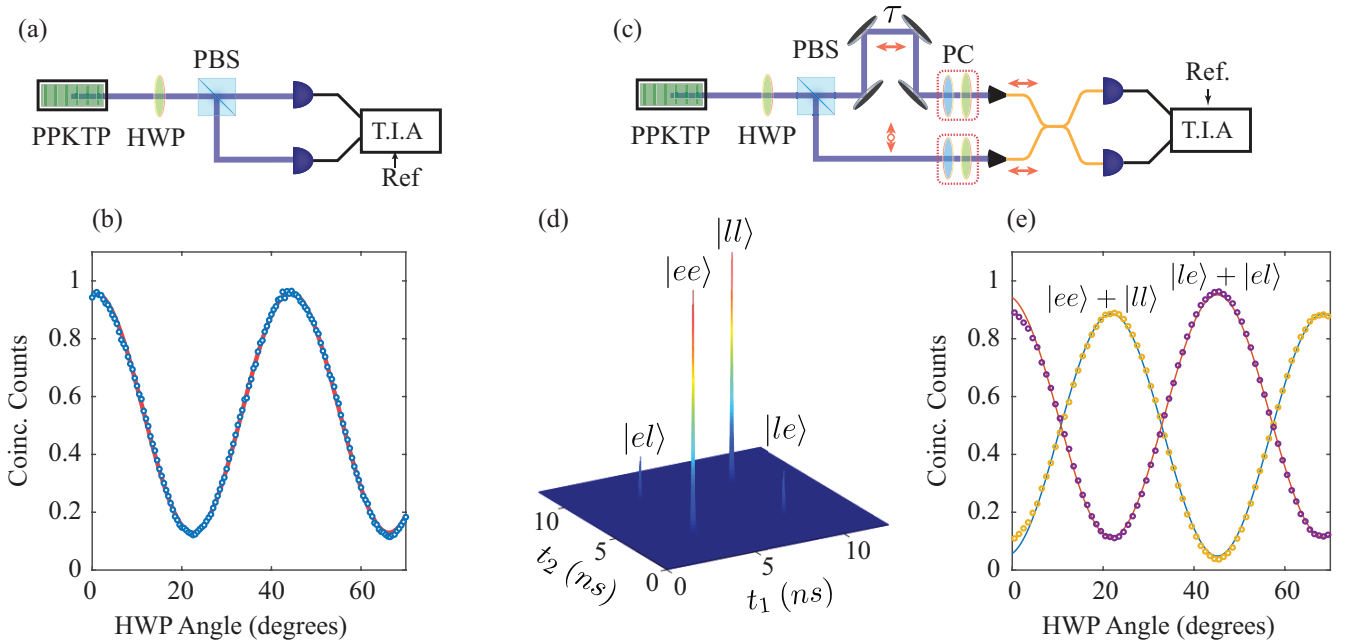
FIG. S6. (a) Experimental setup to verify polarization entanglement. (b) Measured coincidences (blue) as a function of the half-wave plate angle. Red solid line is a cosine fit to the data. (c) Experimental setup to verify time-bin entanglement. (d) Measured joint-temporal intensity at HWP angle of $21.5°$, and (e) coincidences as a function of the half-wave plate angle.

We use a HWP set to $22.5°$ before the PBS of the setup shown in Fig. 1 to generate polarization-entangled entangled photon pairs in the two-photon interference setup [Fig. S6(a)]. The HWP acts as a 50:50 beam splitter in the polarization domain and when the two-photon spectral wave function is symmetric under exchange of photons, generates a polarization-entangled state $|\Psi\rangle = |2\rangle_H |0\rangle_V - |0\rangle_H |2\rangle_V$. To ensure the symmetric wave function, we use a band-pass filter with a bandwidth of ≈ 0.6 nm. To verify this entanglement, we first measure the number coincidences in the two arms of the PBS as a function of the HWP angle [3] [Fig. S6(b)]. The coincidence counts follow a cosine function with a period of $44(2)°$, half of that expected for single

photons. We observe the coincidences to be minimum at $22.5(5)°$, that is, when the two photons are polarization-entangled. The interference visibility is calculated to be $83.0(6)\%$. The low interference visibility is due to temporal walk-off between the H and V photons in the PPKTP crystal which leads to a small temporal distinguishability between the two photons at the HWP.

We also verified the two-photon entanglement using coincidence measurements in the time domain [Fig. S6(c)]. As before, we use a PBS to spatially separate the H and the V polarized photons. We then introduce a large delay (≈ 5 ns) for the V-polarized photons such that they can be temporally distinguished from the H-polarized photons. Subsequently, we change their polarization to H, and combine the two arms using a beam splitter. The H and the V polarization states now correspond to the 'early' and the 'late' time-bin states, respectively. Fig. S6(d) shows the measured temporal correlations between the two output ports of the beam splitter, when the HWP angle is set to $21.5°$. As expected, we observe four coincidence peaks corresponding to the scenarios when both the photons arrive in the 'early' time bin ($e - e$), or in the 'late' time bin ($l - l$), and one photon arrives 'early' and the other 'late' ($e - l$, and $l - e$). Fig. S6(e) shows the total coincidence counts in the $e - e$ and $l - l$ bins, and in the $e - l$ and $l - e$ bins, as a function of the HWP angle. Similar to the polarization resolved measurements, we observe that the coincidence counts follow a cosine curve, and when the HWP angle is $\approx 22.5°$, the two photons are in the time-bin entangled state $|\Psi\rangle = |2\rangle_e |0\rangle_l - e^{-i\varphi} |0\rangle_e |2\rangle_l$. The interference visibility for coincidence counts in the $e - e$ and $l - l$ time bins is $\approx 90\%$ and that for the $e - l$ and $l - e$ time bins is $\approx 79\%$.

S6: STABILIZATION OF THE INTERFEROMETER
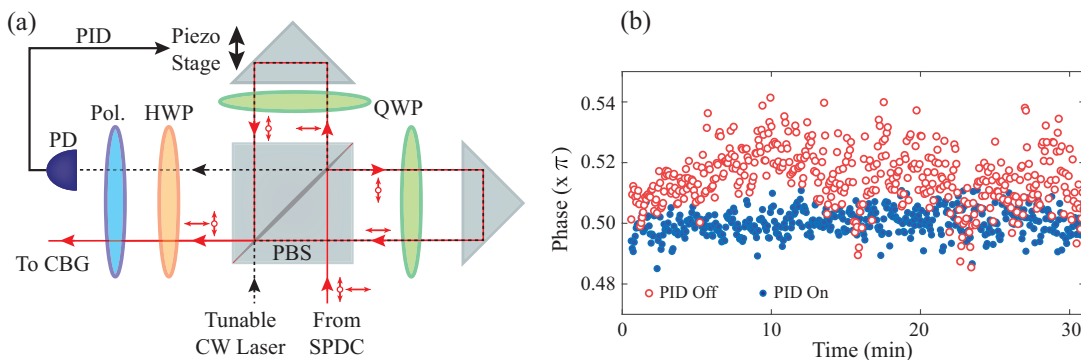
FIG. S7. (a) Experimental setup to stabilize the interferometer. (b) Interferometer stability data with and without PID loop, when the interferometer phase was set to be $\pi/2$.

For measurements using time-bin entangled photons (reported in Fig. 4 of the main text), we used a free-space interferometer [Fig. S7(a)]. The interferometer was actively stabilized using a tunable CW laser and a PID feedback loop. The phase of the interferometer was changed by tuning the CW laser wavelength. During the course of the measurement, the interferometer phase was stable to within ± 1 degree with the active stabilization and ± 2 degrees without active feedback.

S7: EXACT SAMPLING HARDNESS IN THE MULTIPHOTON INTERFERENCE EXPERIMENT

If our setup for the unentangled photons is scaled up to higher number of photons and modes, we sample from an output distribution described in [4]. If the j'th input photon is emitted at time t_j and gets detected at time t, the amplitude for this process is given by $U(t, t_j) = A(t, t_j) \star \mathcal{F}^{-1}\{e^{-i\phi(\omega)}\}$, where $A(t, t_j)$ is the shape of the input photon, the $\star$ operator corresponds to a Fourier convolution, $\mathcal{F}^{-1}$ denotes an inverse Fourier transformation, and $\phi(\omega)$ is the action of a (time-independent) dispersive element. We assume that the action of the dispersive element can be written as $\phi(\omega) = c_0 + c_1(\omega - \omega_0) + c_2(\omega - \omega_0)^2$. The nonlinear dispersion c_2 is what makes the photons spread out in time after passing through this dispersive element. Assuming the input photon wave packet has shape $A(t - t_j) \sim \exp[-\frac{(t-t_j)^2}{\Delta t^2} + i\omega_0(t - t_j)]$, the convolution gives us an amplitude

$$U(t, t_j) = \int_{-\infty}^{\infty} du A(u, t_j) \int_{-\infty}^{\infty} d\omega \exp[-i\phi(\omega) + i\omega(t - u)] \tag{S6}$$

$$\propto \int_{-\infty}^{\infty} du \int_{-\infty}^{\infty} d\omega \exp\left[-\frac{(u-t_j)^2}{\Delta t^2} + i\omega_0(u - t_j) - i\left(c_0 + c_1(\omega - \omega_0) + c_2(\omega - \omega_0)^2\right) + i\omega(t - u)\right]. \tag{S7}$$

This simplifies to $U(t, t_j) = \psi(t - t_j)e^{i\omega_0 t + 4ic_2 t^2}$, where

$$\psi(t - t_j) \propto \exp\left[-\frac{(t - t_j - c_1)^2}{\Delta t^4 + 16c_2^2}(\Delta t^2 - 4ic_2)\right]. \tag{S8}$$

This amplitude $U(t, t_j)$ is also the expression for the matrix element of the linear-optical unitary once the temporal modes have been discretized by integrating over a small enough window of size t_s: $a_{t_j}^\dagger = \frac{1}{\sqrt{t_s}} \int_{t_j}^{t_j + t_s} a^\dagger(t)\mathrm{d}t$.

Now, when the input has photons emitted at times $\{0, \delta t, 2\delta t, \ldots\}$, and the detections at the output occur at times $\{t_1, t_2, \ldots\}$, the total amplitude for the output state is given by

$$\mathrm{Per} \begin{bmatrix} \psi(t_1)e^{i\omega_0 t_1 + 4ic_2 t_1^2} & \psi(t_1 - \delta t)e^{i\omega_0(t_1 - \delta t) + 4ic_2(t_1 - \delta t)^2} & \psi(t_1 - 2\delta t)e^{i\omega_0(t_1 - 2\delta t) + 4ic_2(t_1 - 2\delta t)^2} & \cdots \\ \psi(t_2)e^{i\omega_0 t_2 + 4ic_2 t_2^2} & \psi(t_2 - \delta t)e^{i\omega_0(t_2 - \delta t) + 4ic_2(t_2 - \delta t)^2} & \psi(t_2 - 2\delta t)e^{i\omega_0(t_2 - 2\delta t) + 4ic_2(t_2 - 2\delta t)^2} & \cdots \\ \vdots & \vdots & \ddots & \cdots \end{bmatrix}, \tag{S9}$$

where the symbol "Per" denotes the permanent of a matrix. In the two-photon case, one may verify that this gives fringes in the output distribution over (t_1, t_2) with period $2\pi/(8c_2\delta t)$, which translates to the fringes in the measured frequencies (ω_1, ω_2).

We now analyze the complexity of sampling from the output distribution for the n-photon case. The matrix in Eq. S9 may be viewed as a submatrix of a bigger unitary matrix that has encoded in it all possible photon emission times and all possible detection times. This bigger unitary matrix has several symmetries since its columns differ only by translation in time and a phase. Further, it is approximately banded since the matrix elements fall off as a Gaussian.

The output distribution can be interpolated from being completely distinguishable ($c_2 \to 0$) to indistinguishable ($c_2^2 \gg \delta t$). In the indistinguishable regime, the output distribution can be hard to exactly sample from. Consider an event where the output photons are all detected at similar times, i.e. they are all within a small window around c_1. This event is unlikely since the photons that come later on have an exponentially suppressed amplitude for being detected at time c_1: $|U(c_1, k\delta t)| \sim \exp[-\frac{k^2\delta t^2}{\Delta t^2 + 16c_2^2/\Delta t^2}]$, but the unlikeliness of such an outcome does not hamper a proof of exact sampling hardness.

The output amplitude for such an event is now given by the permanent of a matrix where the matrix elements U_{ij} behave as $|U_{ij}| \sim \exp[-j^2/w]$, with $w = (\Delta t^2 + 16c_2^2/\Delta t^2)/\delta t^2$. The dependence on the row index i is weak since all the output times were chosen to be around t_1. If one factors out this dependence of the columns to define a new matrix $R_{ij} = U_{ij}/\exp[-j^2/w]$, then one gets a matrix whose entries have uniform absolute values on average. It is plausible that randomly choosing the output time labels $(t_1, t_2, \ldots) = (c_1 + x_1, c_1 + x_2, \ldots)$ where x_i's are random variables would give a sufficiently random matrix R. Aaronson and Arkhipov [?] gave evidence that finding the permanent of a random matrix whose entries are random Gaussians is #P-hard on average. The permanent of U is simply $\exp[-n/w \sum_j j^2]\mathrm{Per}\, R$, which is a known factor. Hence $\mathrm{Per}\, U$ is as hard to compute as $\mathrm{Per}\, R$, which is likely #P-hard on average. However, this does not rule out the possibility of an efficient approximate sampling algorithm that exploits the Gaussian fall-off in the matrix elements of the unitary.

---

[1] V. Giovannetti, L. Maccone, J. H. Shapiro, and F. N. C. Wong, Phys. Rev. A **66**, 043813 (2002).

[2] W. P. Grice and I. A. Walmsley, Phys. Rev. A **56**, 1627 (1997).

[3] S. Slussarenko, M. M. Weston, H. M. Chrzanowski, L. K. Shalm, V. B. Verma, S. W. Nam, and G. J. Pryde, Nature Photonics **11**, 700 (2017).

[4] M. Pant and D. Englund, Phys. Rev. A **93**, 043803 (2016).